Interaction of Superinertial Waves with Submesoscale Cyclonic Filaments in the North Wall of the Gulf Stream

DANIEL B. WHITT

National Center for Atmospheric Research, Boulder, Colorado

LEIF N. THOMAS

Earth System Science Department, Stanford University, Stanford, California

JODY M. KLYMAK

School of Earth and Ocean Sciences, University of Victoria, Victoria, British Columbia, Canada

CRAIG M. LEE AND ERIC A. D'ASARO

Applied Physics Laboratory, University of Washington, Seattle, Washington

(Manuscript received 13 April 2017, in final form 15 August 2017)

ABSTRACT

High-resolution, nearly Lagrangian observations of velocity and density made in the North Wall of the Gulf Stream reveal banded shear structures characteristic of near-inertial waves (NIWs). Here, the current follows submesoscale dynamics, with Rossby and Richardson numbers near one, and the vertical vorticity is positive. This allows for a unique analysis of the interaction of NIWs with a submesoscale current dominated by cyclonic as opposed to anticyclonic vorticity. Rotary spectra reveal that the vertical shear vector rotates primarily clockwise with depth and with time at frequencies near and above the local Coriolis frequency f. At some depths, more than half of the measured shear variance is explained by clockwise rotary motions with frequencies between f and $1.7f$. The dominant superinertial frequencies are consistent with those inferred from a dispersion relation for NIWs in submesoscale currents that depends on the observed aspect ratio of the wave shear as well as the vertical vorticity, baroclinicity, and stratification of the balanced flow. These observations motivate a ray tracing calculation of superinertial wave propagation in the North Wall, where multiple filaments of strong cyclonic vorticity strongly modify wave propagation. The calculation shows that the minimum permissible frequency for inertia–gravity waves is mostly greater than the Coriolis frequency, and superinertial waves can be trapped and amplified at slantwise critical layers between cyclonic vortex filaments, providing a new plausible explanation for why the observed shear variance is dominated by superinertial waves.

1. Introduction

Near-inertial waves (NIWs) and inertia–gravity waves (IGWs) with frequency close to the local Coriolis frequency f interact strongly with mesoscale- and submesoscale-balanced currents for several reasons. Unlike higher-frequency IGWs, the lateral group velocity of NIWs is small compared to the speed of balanced currents; consequently, the "crests" and "troughs" of NIWs can be strongly distorted by mesoscale and submesoscale shears (Bühler and McIntyre 2005). In addition, the vorticity associated with these shears shifts the net spin of the fluid away from Earth's rotation, leading to marked changes in the dispersion and polarization relations of NIWs. For example, in a geostrophic current $u_g(y, z)$, the vertical vorticity $\zeta_g = -\partial u_g/\partial y$ modifies the effective Coriolis frequency $f_{\text{eff}} = f\sqrt{(1 + \text{Ro}_g)}$ (where $\text{Ro}_g = \zeta_g/f$ is the Rossby number), which constrains the minimum frequency of the NIWs. Furthermore, horizontal vorticity associated with thermal wind shear $\partial u_g/\partial z$ lowers the minimum frequency of NIWs from f_{eff} to

Corresponding author: Daniel B. Whitt, dwhitt@ucar.edu

DOI: 10.1175/JPO-D-17-0079.1

© 2018 American Meteorological Society. For information regarding reuse of this content and general copyright information, consult the AMS Copyright Policy (www.ametsoc.org/PUBSReuseLicenses).

$$\omega_{\min} = f\sqrt{\left(\frac{f_{\text{eff}}}{f}\right)^2 - \frac{1}{\text{Ri}_g}}, \quad (1)$$

where $\text{Ri}_g = N^2/(\partial u_g/\partial z)^2$ is the Richardson number of the geostrophic flow, and N is the buoyancy frequency (Mooers 1975; Kunze 1985). The modifications to the properties of NIWs are thus particularly pronounced in submesoscale-balanced currents since they are characterized by Richardson and Rossby numbers that are order one.

In this submesoscale regime, NIWs can exhibit unexpected behavior. For example, NIW velocity hodographs do not trace inertial circles but are instead elliptical and, for a given wave frequency, the direction of energy propagation is symmetric about the slope of isopycnals not the horizontal and approaches the isopycnal slope as the frequency nears $\omega_{\min}$ (Mooers 1975; Whitt and Thomas 2013). This unusual wave physics can facilitate energy transfers between NIWs and balanced currents (Thomas 2012) and allow for the formation of critical layers along the sloping isopycnals of fronts (Whitt and Thomas 2013).

There have been several field campaigns designed to study NIW-balanced flow interactions in the mesoscale regime, that is, with $\text{Ro}_g \lesssim 0.1$ and $\text{Ri}_g \gg 1$, that support theoretical predictions of trapped subinertial waves in regions of anticyclonic vorticity and the development of vertical critical layers (e.g., Kunze and Sanford 1984; Kunze 1986; Mied et al. 1987; Kunze et al. 1995). In this article we present observations of NIWs in the North Wall of the Gulf Stream, where the balanced flow has Rossby numbers that exceed one and Richardson numbers that drop below one (Klymak et al. 2016; Thomas et al. 2016). The observations were collected as part of the Scalable Lateral Mixing and Coherent Turbulence (LatMix) 2012 field campaign (19 February–17 March 2012), the goal of which was to study submesoscale processes and their effect on mixing in the Gulf Stream and northern Sargasso Sea. The objective of this paper is to quantitatively characterize the NIWs and the relevant properties of the medium in which they propagate (e.g., Ro and Ri) in a high-resolution Lagrangian survey of velocity and density in the upper pycnocline of the Gulf Stream Front obtained during the LatMix campaign. In addition, we will use the theory of Whitt and Thomas (2013) for NIWs in submesoscale fronts to interpret the prominent features of the wave field seen in the observations.

2. Observed frontal structure

a. Data from ships and towed profilers

Observations were made while underway on two global class research vessels, R/V *Knorr* and R/V *Atlantis*, traveling at approximately 8 kt (1 kt = 0.51 m s^{-1}). Both ships were equipped with two shipboard-mounted acoustic Doppler current profilers (ADCPs). A 300-kHz Teledyne RDI Workhorse sampled the top 100–150 m with 4-m vertical resolution, while a 75-kHz Teledyne RDI Ocean Surveyor surveyed the top 500–600 m with 8-m vertical resolution. In addition, the R/V *Knorr* was equipped with a towed MacArtney TRIAXUS that undulated between the surface and 200 m to provide profiles of temperature, conductivity, and pressure along a sawtooth pattern with a resolution of approximately 1 km in the direction of travel. The R/V *Atlantis* was equipped with a Rolls Royce moving vessel profiler (MVP) with a free-falling AML Oceanographic micro-CTD to provide vertical profiles of temperature, conductivity, and pressure, again with a resolution of approximately 1 km in the direction of travel.

Part of the analysis requires velocity and density interpolated to the same time-depth grid, covering the top 200 m. The velocity data for these grids are obtained by merging data from the 300- and 75-kHz ADCPs on each ship and interpolating that data to the density grid derived from the profiler data collected on that ship. In particular, current measurements are first averaged over approximately 1 km in the direction of travel in depth bins of 4 (300 kHz) and 8 m (75 kHz). Then, the data from the 75-kHz ADCP are linearly interpolated to the 1 km by 4 m 300-kHz grid and gaps in the 300-kHz data are filled with the interpolated 75-kHz data. The resulting merged velocity data are then smoothed with a two-dimensional Gaussian kernel with a standard deviation of 4 m in depth and approximately 1 km in the direction of ship travel. The half-power wavelengths of this two-dimensional Gaussian kernel are 30 m in the vertical and approximately 7.5 km in the direction of ship travel (i.e., 30 min at 8 kt). Finally, the smoothed velocity profiles are linearly interpolated (along the ship track) to the positions of the density profiles.

The density is gridded slightly differently, depending on the vessel/instrument. Each TRIAXUS profile is averaged into 2-m vertical bins (ups and downs are included as separate profiles). The horizontal position/time of each profile is defined by the ship position/time at the midpoint of each TRIAXUS profile. For example, gray dots in Fig. 3a (shown below) mark the ship positions at the midpoint of each TRIAXUS profile in one section across the Gulf Stream. Each downgoing vertical MVP profile is averaged into 1-m vertical bins at a given position/time (upward profiles from the MVP are excluded). For example, gray dots in Fig. 2a (shown below) mark the MVP vertical profile locations in one section across the Gulf Stream. The gridded density

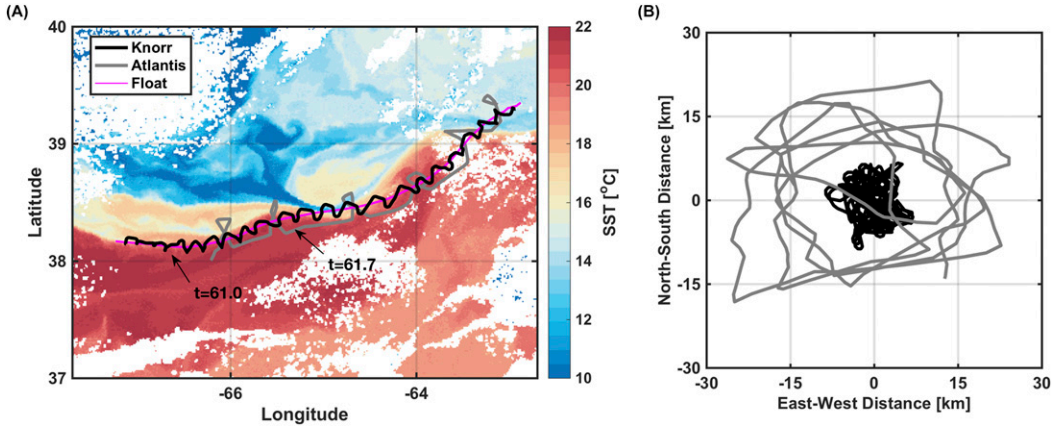

FIG. 1. (a) Sea surface temperature (color) and the paths of the R/V *Knorr* (black) and R/V *Atlantis* (gray). (b) The position of the observational platforms relative to the Lagrangian float [magenta line in (a)] over the duration of the drift. The approximate locations of the ships and float at yearday 61 and 61.7 are marked with arrows.

from each profiler is then filtered by applying the same two-dimensional Gaussian smoother that was applied to the velocity data, and the resulting filtered density is linearly interpolated (in depth) to the 4-m bins of the velocity grid.

After this filtering and gridding, density and velocity are collocated at the horizontal positions of the density profiles in uniform 4-m vertical bins, and features with wavelengths less than about 30 m in the vertical and 7.5 km in the direction of ship travel have been filtered out of both the density and velocity datasets.

b. *Experimental description and observed frontal structure*

Measurements focused on the North Wall of the Gulf Stream, past the point where it separates from Cape Hatteras, North Carolina, between 38° and 40°N and 60° and 70°W. Here, cold subpolar water and warm subtropical water converge to form a strong front. The campaign was broken into a series of drifts, each following an acoustically tracked Lagrangian float (D'Asaro 2003) placed in the surface mixed layer in the strongest part of the front for 2 to 4 days. In each drift, the ships made repeated frontal cross sections following the float (e.g., Fig. 1). The float was tracked using a transducer pole, which was mounted on the R/V *Knorr*, extended 2 m below the keel, and provided a maximum range of about 4 km. To track the float accurately, the R/V *Knorr* remained within about 5 km of the float position. The tracking equipment is otherwise similar to that used in D'Asaro et al. (2011), and the uncertainties associated with the float position estimates are thought to be small compared to other uncertainties in the analysis.

In this paper, attention is focused on the second drift, which occurred from 1 March through 3 March 2012 (yeardays 60 through 62), near the strongest part of the front (Fig. 1a). While the *Atlantis* made wider ~30-km cross sections around the float, the *Knorr* made narrower ~10-km cross sections, closely following the float (Fig. 1b). The survey strategy involved intensive sampling of the water around a Lagrangian float in the mixed layer in an attempt to minimize the convoluting effects of advection on the analysis. But, it is important to note the observations were obtained in a region of strong lateral and vertical gradients in velocity, and therefore the observed fluid is not exactly in a Lagrangian frame of reference at all depths and cross-stream locations observed.

A typical cross-front section from the *Atlantis* (Fig. 2) exhibits a strong surface-intensified jet with velocities exceeding $2\,\mathrm{m\,s^{-1}}$ in the streamwise direction x, order-one vorticity Rossby numbers ($\mathrm{Ro} = \zeta/f \approx -\partial u/\partial y/f$, where f is the Coriolis frequency, u is the along-stream velocity, and y points in the cross-stream direction), isopycnal slopes s_b of order 0.01, and geostrophic Richardson numbers Ri_g ranging from 1 to 10. To estimate Ro and Ri_g, the associated gradients are calculated using central differences over approximately 2 km in the horizontal and 8 m in the vertical, but variability on scales less than about 30 m in the vertical and 7.5 km in the horizontal is suppressed by the processing (see section 2a). In any case, the resolved flow is in the submesoscale part of (Ro, Ri) parameter space suggesting that if there are NIWs in the current they should be substantially modified by its vorticity and baroclinicity. As described in the next

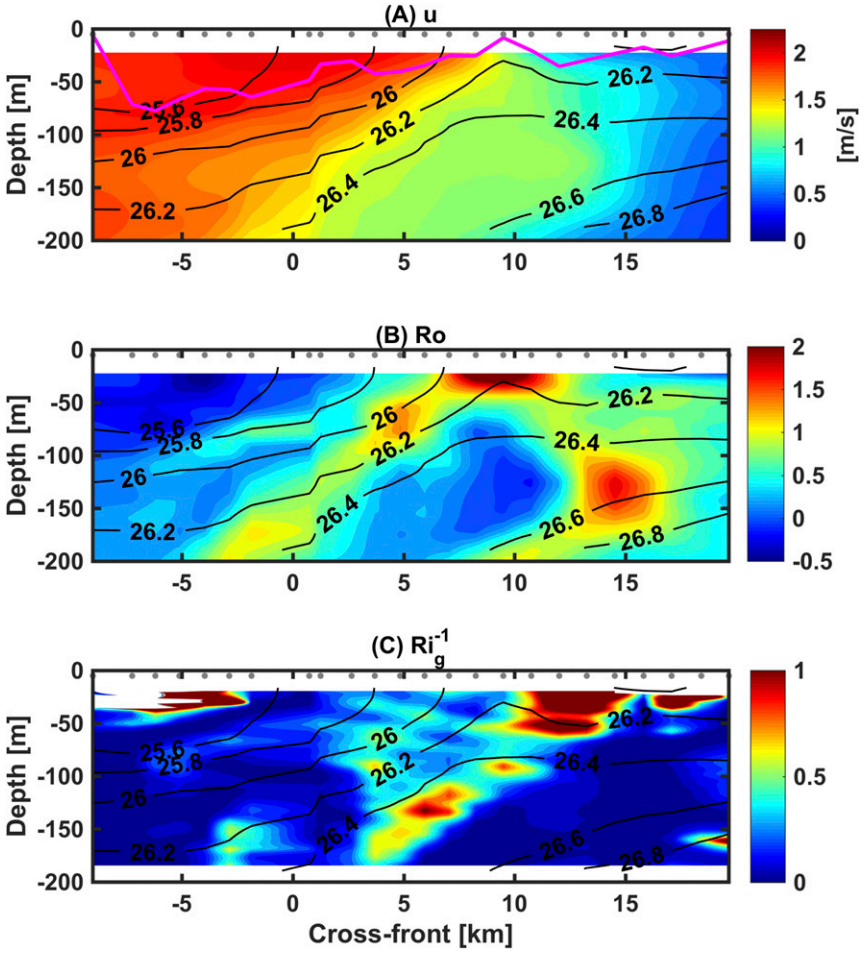

FIG. 2. Data from the second *Atlantis* section obtained at about yearday 61.3 at a mean latitude and longitude of 38.2°N, 66.1°W; see Fig. 1a. Cross-front/depth maps of (a) streamwise velocity u, (b) vorticity Rossby number $\mathrm{Ro} = -\partial u/\partial y/f$, and (c) inverse geostrophic Richardson number $\mathrm{Ri}_g^{-1} = (\partial b/\partial y)^2/(f^2 \partial b/\partial z)$ show that the observations are in a submesoscale front, that is, where $\mathrm{Ro} \sim \mathrm{Ri}_g^{-1} \sim 1$. The mixed layer depth, defined by a 0.03 kg m^{-3} density threshold, is indicated by a magenta line in (a). Note that the coordinate system is rotated so that the streamwise velocity u is defined to be the velocity parallel to the float path, the coordinate y represents the cross-front distance in the direction perpendicular to the float path, and $y = 0$ km denotes the cross-front location of the float path. Each gray dot at $z \approx 0$ m indicates the location of an MVP profile.

section, there were indeed features in the observed flow field during the drift with properties that are consistent with NIWs, giving us the opportunity to study the interaction of the waves with a submesoscale current.

3. Observations of near-inertial shear

a. Structure and evolution of the vertical shear

Banded patterns of strong vertical shear $\partial \mathbf{u}/\partial z$ [where $\mathbf{u} = (u, v)$ is the horizontal velocity vector] were observed during the drift. To analyze these features, we rotate the coordinate system so that (x, y) denotes the streamwise and cross-stream directions respectively, and x is defined to point in the direction of the local float path, whereas y points in the direction perpendicular to the local float path.

Sections of the streamwise and cross-stream shear, $\partial u/\partial z$ and $\partial v/\partial z$, respectively, reveal shear anomalies (i.e., relative to a linear fit in z) that are arranged into banded structures parallel to slanted isopycnals (Figs. 3a,b). The shear anomalies have a dominant vertical wavelength between 50 and 100 m and magnitudes of up to 0.005 s^{-1}, which is comparable to the depth-averaged alongfront

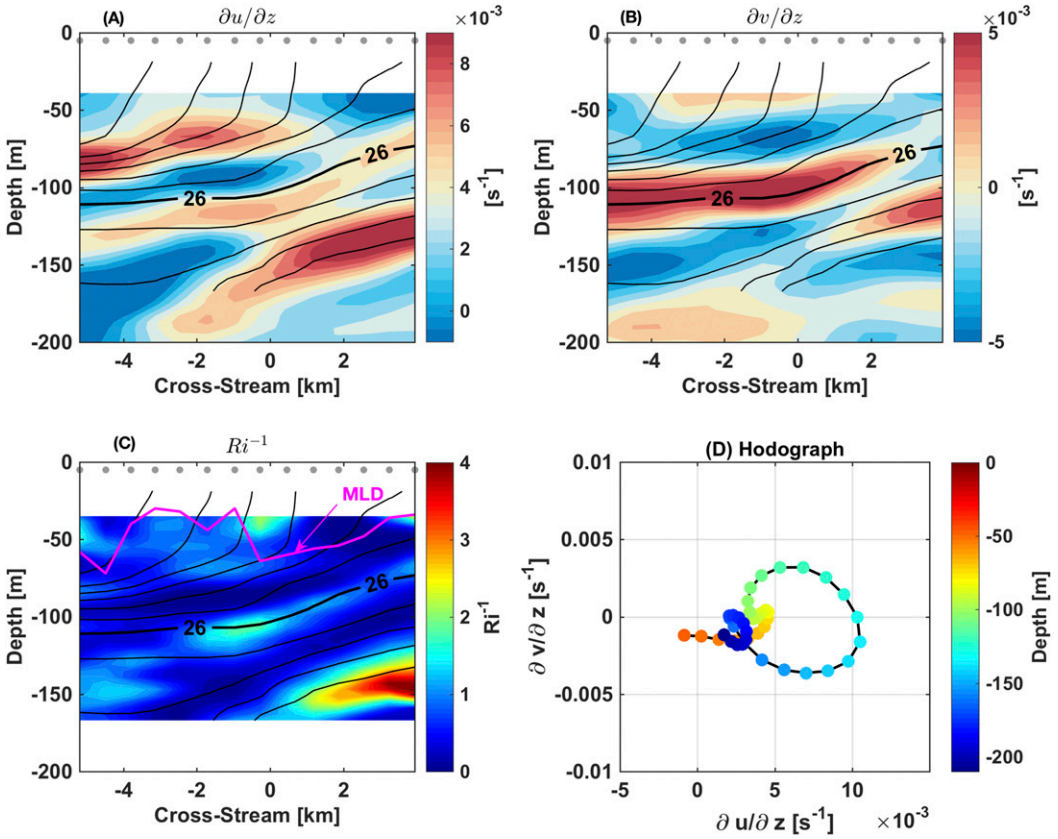

FIG. 3. Data from the fifth *Knorr* section shown in Fig. 1a, which were obtained at yearday 61.1 at a mean latitude and longitude of 38.1°N, 66.3°W. Maps are presented of (a) the streamwise component of the vertical shear $\partial u/\partial z$, (b) the cross-stream component of the vertical shear $\partial v/\partial z$, and (c) the inverse Richardson number $\mathrm{Ri}^{-1} = [(\partial u/\partial z)^2 + (\partial v/\partial z)^2]/\partial b/\partial z$. Density contours are superimposed with a spacing of 0.1 kg m^{-3}. The mixed layer depth, defined by a 0.03 kg m^{-3} density threshold, is indicated by a magenta line in (c). (d) The hodograph of the shear vector $\partial \mathbf{u}/\partial z$ averaged laterally between $y = 1$ and 4 km rotates primarily clockwise with depth. Note that the coordinate system is as in Fig. 2, and each gray dot at $z \approx 0$ m indicates the location of a TRIAXUS profile.

shear (Figs. 3a,b). However, the associated velocity anomalies, $\mathbf{u}_a \sim (1/m)(\partial \mathbf{u}_a/\partial z) \lesssim 0.1\,\mathrm{m\,s^{-1}}$, are much smaller than the velocity of the depth-averaged alongfront flow of ~1–2 m s^{-1} (Fig. 2a). Yet, the shear anomalies are sufficiently intense to be associated with banded patterns in the inverse Richardson number $\mathrm{Ri}^{-1} = |\partial \mathbf{u}/\partial z|^2/N^2$, which often exceeds 1 and approaches 4 in some places (Fig. 3c). These high values of Ri^{-1} occur despite the smoothing applied during data processing and instrument resolution/noise effects, which all tend to cause these estimates of Ri^{-1} to be biased very low at the 8-m vertical scale on which the gradients are calculated and to be biased slightly low (by perhaps a factor of 2) at 30-m vertical scales [see Alford and Pinkel (2000) for a useful discussion of these biases]. Finally, the shear vector is polarized in z so that the direction of the shear vector rotates clockwise with increasing depth (i.e., decreasing z; see Fig. 3d).

The time series of the wind stress together with maps of the streamwise and cross-stream vertical shear observed from the ships at points near the float path illustrate the temporal evolution of the banded shear and the atmospheric forcing during the drift (Fig. 4). Individual time series of the shear averaged between −45 and −65 m and −65 and −85 m further highlight this evolution (Fig. 5). The time series show that the shear anomalies evolve significantly with time/downstream position at essentially all depths/isopycnals during the drift. Yet, the shear anomalies exhibit a consistent dominant vertical wavelength between 50 and 100 m and achieve a similar maximum amplitude of 0.005 s^{-1}, which is similar in magnitude to the depth-averaged alongfront shear, throughout the drift. Likewise, the shear anomalies are associated with regions of low Richardson number $\mathrm{Ri} \approx 1$ below the mixed layer at various times throughout the drift (Fig. 4d).

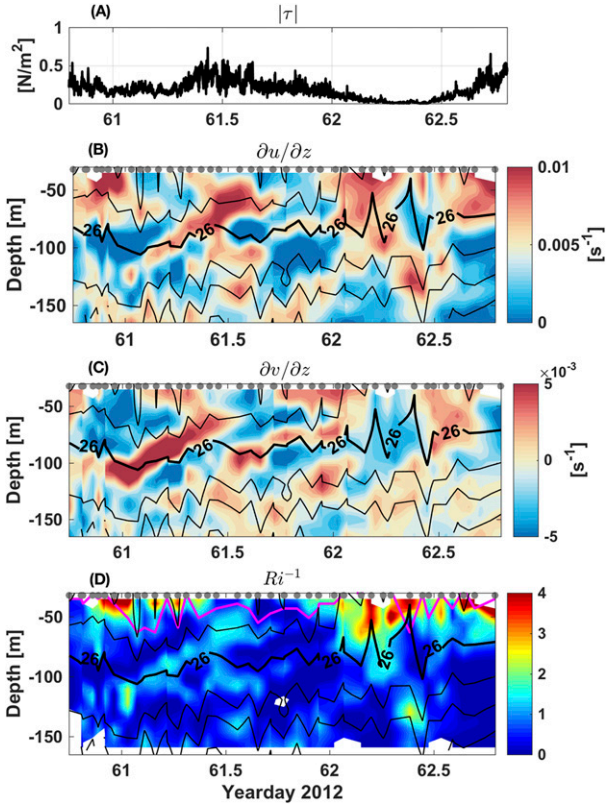

FIG. 4. Several time series of data collected along the whole drift. (a) The 1-min moving average of the wind stress derived from observations of wind speed at a meteorological station on the *Knorr* and converted to a stress using the algorithm of Large and Pond (1981). (b) The streamwise component of the vertical shear $\partial u/\partial z$, (c) the cross-stream component of the vertical shear $\partial v/\partial z$, and (d) the inverse Richardson number $\mathrm{Ri}^{-1} = [(\partial u/\partial z)^2 + (\partial v/\partial z)^2]/\partial b/\partial z$. (b)–(d) are derived from *Knorr* ADCP and TRIAXUS data. Density contours are superimposed with a spacing of 0.1 kg m^{-3} in each plot. The mixed layer depth, defined by a 0.03 kg m^{-3} density threshold, is indicated by a magenta line in (d). However, only those observations within 350 m of the float path (the magenta line in Fig. 1a) are included here; gray dots indicate the location of TRIAXUS profiles where this condition is met and data are included.

The structure and time/downstream evolution of the vertical shear field illustrated in Figs. 2–5 suggests qualitatively that the shear is associated with downward-propagating NIWs that are potentially modified by the vorticity and baroclinicity of the Gulf Stream, as described by Whitt and Thomas (2013). In particular, the temporal variability of the observed shear appears to be dominated by oscillations with frequencies that are slightly higher than the local Coriolis frequency $f \approx 9 \times 10^{-5}\,\mathrm{s}^{-1}$ (the local inertial period corresponds to ~0.8 days). In addition, lines of constant shear anomaly propagate upward with time, which is consistent with downward-propagating NIW physics. To test this hypothesis more quantitatively, rotary vertical wavenumber and frequency spectra will be used to decompose the shear variance into clockwise and counterclockwise components and estimate the dominant wave frequency in sections 3b and 3c, and the results will be compared to the theoretical predictions of Whitt and Thomas (2013) in sections 4–5.

b. Rotary vertical wavenumber spectra

The vertical variation of $\partial\mathbf{u}/\partial z$ seen in Fig. 3 suggests that the shear vector rotates primarily clockwise with increasing depth at that location. A quantitative estimate of the shear vector's average sense of rotation with depth along the float path is derived from the rotary components of the Froude number vertical wavenumber spectrum [i.e., a buoyancy frequency normalized shear spectrum (e.g., Munk 1981; Alford and Gregg 2001; Rainville and Pinkel 2004)]. We calculate Froude number spectra rather than shear spectra because the former provides more information about the local stability of the waves, and observations collected at locations with different stratifications can be more easily compared with each other (Munk 1981).

The Froude wavenumber spectra are constructed as follows: For each profile of density made within 350 m of the float path, profiles of shear anomaly

$$\frac{\partial \mathbf{u}_a}{\partial z}(z) = \left[\frac{\partial u_a}{\partial z}(z), \frac{\partial v_a}{\partial z}(z)\right]$$

are created by subtracting a linear fit from each component of the full shear vector over the depth range $(z_0 - L_z) \le z \le z_0$, where $z_0 = -29$ m and $L_z = 160$ m. The full shear vector is constructed from the smoothed velocity field described in section 2a. These profiles $\partial\mathbf{u}_a/\partial z$ are normalized by dividing by the depth-averaged buoyancy frequency $\overline{N}(t)$, which is calculated over the same depth range as the shear and varies by 40%, from 0.0056 to 0.0079 s^{-1}, during the drift. The two components of the shear are then combined into a complex Froude number profile:

$$\mathrm{Fr}(z) = \frac{\dfrac{\partial u_a}{\partial z}(z) + i\dfrac{\partial v_a}{\partial z}(z)}{\overline{N}}, \qquad (2)$$

where $i = \sqrt{-1}$. A 20% tapered cosine (Tukey) window is applied to $\mathrm{Fr}(z)$ and then the discrete Fourier transform $\widehat{\mathrm{Fr}}(m_k) = \Delta z \sum_{n=0}^{2M-1} \mathrm{Fr}(z_n) e^{-im_k z_n}$ is computed using the fast Fourier transform algorithm for each wavenumber $\pm m_k = \pm k\Delta m$ (where $k = -M, \ldots, -1, 0, 1, \ldots, M-1$, $\Delta m = 2\pi/L_z$ is the smallest resolvable

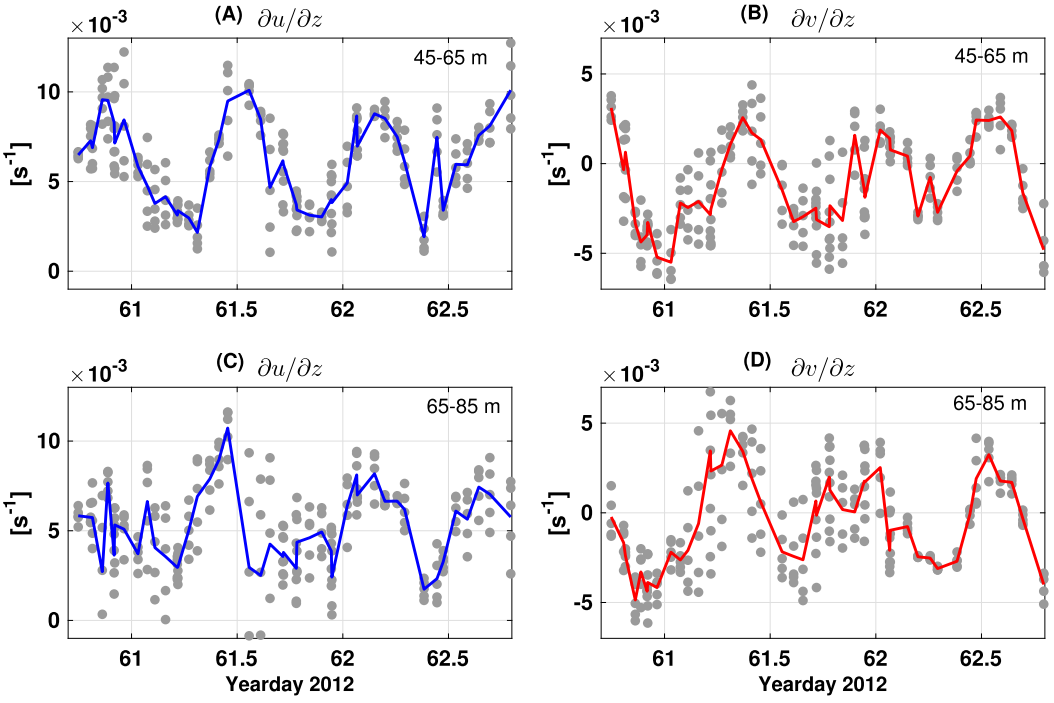

FIG. 5. (a),(c) The streamwise vertical shear and the (b),(d) cross-stream vertical shear observed (top) between 45- and 65-m depth and (bottom) between 65- and 85-m depth along the float path. As in Fig. 4, the observations are from the *Knorr* but restricted to cross-stream positions within 350 m of the float path. Data are binned into 4-m depth bins, so there are five time series in each panel. Colored lines mark the average of all five depth bins at each time.

wavenumber, M is half the number of observations in the depth domain, $\Delta z = 4$ m is the vertical grid spacing, and the z_n are the $2M$ discrete depths). The resulting transforms are rescaled to account for the variance reduction caused by windowing and are most accurate at vertical wavelengths between 80 and 40 m. This is because energy in the smallest resolved wavenumber Δm is more strongly damped by the windowing, whereas the higher wavenumbers are more severely contaminated by instrument noise, resolution effects, and the smoothing during processing (see section 2a). A useful discussion of the relevant sampling issues related to shipboard ADCPs can be found in the appendix of Alford and Gregg (2001). Because the data presented here are derived from two ADCPs with different vertical resolutions, no attempt is made to scale up the resulting Froude wavenumber spectra to account for ADCP resolution or smoothing effects, both of which may conspire to reduce the reported Froude wavenumber spectra by as much as a factor of 2 at a vertical wavelength of 40 m but will impact the positive and negative vertical wavenumbers m_+ and m_- equally. The positive and negative vertical wavenumbers m_+ and m_- represent the clockwise (CW) and counterclockwise (CCW) parts of the rotary Froude wavenumber spectrum, respectively, which are given by

$$\widehat{\mathrm{Fr}}^2_{\mathrm{CW}}(m_+) = \frac{\left\langle \widehat{\mathrm{Fr}}(m_+)\widehat{\mathrm{Fr}}(m_+)^c \right\rangle}{2\pi L_z}, \quad \text{and} \tag{3}$$

$$\widehat{\mathrm{Fr}}^2_{\mathrm{CCW}}(m_-) = \frac{\left\langle \widehat{\mathrm{Fr}}(m_-)\widehat{\mathrm{Fr}}(m_-)^c \right\rangle}{2\pi L_z}, \tag{4}$$

where the superscript c denotes the complex conjugate, and $\langle\cdot\rangle$ denotes the ensemble average over all vertical profiles along the float path. The spectra are normalized by dividing by $2\pi L_z$ so that

$$\overline{\mathrm{Fr}^2} = \frac{\Delta z}{L_z}\sum_{n=0}^{2M-1}\frac{\frac{\partial u_a(z_n)}{\partial z}^2 + \frac{\partial v_a(z_n)}{\partial z}^2}{\overline{N}^2} \approx \Delta m \sum_{k=-M}^{M-1}\widehat{\mathrm{Fr}}^2(m_k) \tag{5}$$

by Parseval's theorem. The contribution from different wavenumbers m_k to the depth-averaged $\overline{\mathrm{Fr}^2}$ can then be estimated by integrating over a subset of the resolved vertical wavenumbers m_k (e.g., Munk 1981). Confidence intervals for the average spectral estimates [(3)–(4)] are derived from a χ^2 distribution. The effective number of independent observations used to calculate the confidence intervals (nine in this case) is estimated by dividing the length of the drift by the largest integral time scale calculated from the temporal correlation function of $\widehat{\mathrm{Fr}}^2(m_k, t)$ (e.g., D'Asaro and Perkins 1984; Emery and Thomson 2001).

The rotary components of the Froude wavenumber spectra (plotted in Fig. 6) show that the average CW Froude variance is 2–5 times greater than the average CCW Froude variance at vertical wavelengths of 40 to 80 m. The enhanced CW Froude variance is in contrast to the canonical internal wave continuum, in which waves propagate upward and downward in equal proportion (e.g., Garrett and Munk 1972), and is consistent with the presence of energetic and coherent, downward-propagating NIWs (e.g., Leaman and Sanford 1975; Kunze and Sanford 1984; Mied et al. 1987; Alford and Gregg 2001; Shcherbina et al. 2003; Inoue et al. 2010; Thomas et al. 2010; Jaimes and Shay 2010). However, having said this, this conclusion is derived using the polarization relations of NIWs in the absence of a background flow. Whitt and Thomas (2013) show that submesoscale fronts strongly modify the polarization of NIWs, which can affect the ratio of CW to CCW Froude variance for downward-propagating NIWs. We will explore this physics in section 4.

c. *Rotary frequency spectra*

The temporal variation of the shear vector is most wavelike just below the base of the mixed layer. There, the shear varies nearly sinusoidally with a similar amplitude and a fixed phase relationship between the streamwise shear $\partial u/\partial z$ and cross-stream shear $\partial v/\partial z$ (Fig. 5). In particular, $\partial v/\partial z$ leads $\partial u/\partial z$ by a quarter of a cycle (Fig. 5), indicating that the shear vector rotates clockwise with increasing time, which is consistent with the dynamics of NIWs in the Northern Hemisphere (e.g., Gonella 1972).

To obtain quantitative measures of the frequencies and amplitudes of the two rotary components of the observed shear we calculate rotary frequency spectra from the shear vector time series collected within 350 m of the float path. To do so, we define the complex vector time series of the Froude number

$$\mathrm{Fr}(t) = \frac{\frac{\partial u_a}{\partial z}(t) + i\frac{\partial v_a}{\partial z}(t)}{\overline{N}} \tag{6}$$

at each depth bin z, where $\partial \mathbf{u}_a/\partial z(t)$ is the shear anomaly that is constructed by removing a linear fit (in time) from each component of the shear vector. After dividing by the time-mean $\overline{N}(z)$ in each depth bin, which varies by 29% from 0.0063 to 0.0081 s^{-1} over all z between $z = -41$ and -189 m, the resulting time series $\mathrm{Fr}(t)$ is windowed with a 20% tapered cosine (Tukey) window. Since the TRIAXUS profiles within 350 m of the float path are rather unevenly spaced in time, a least squares approach (e.g., Lomb 1976; Scargle 1982) is used to estimate the Fourier transform $\widehat{\mathrm{Fr}}(\omega_k)$ for each frequency

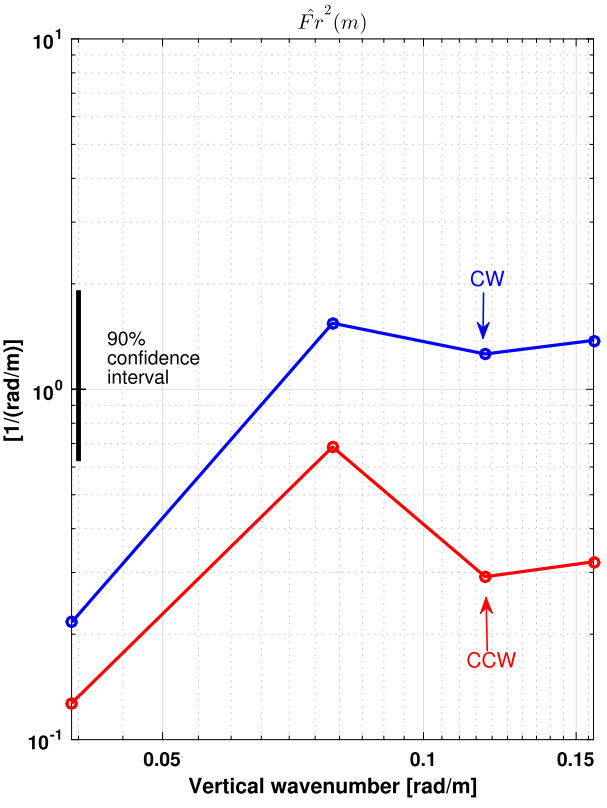

FIG. 6. The float path average CW and CCW rotary components of the Froude number spectrum $\widehat{\mathrm{Fr}}^2(m)$ as a function of the angular vertical wavenumber m over the depth range $z = -29$ to -189 m. Only the data shown in Fig. 4 are used in the calculation; hence, this average represents data within 350 m of the float path. The vertical wavelengths $2\pi/m$ that are shown range from 40 to 160 m. The 90% confidence interval is shown in black.

$\omega_k = k\Delta\omega$, where $k = -M, \ldots, -1, 0, 1, \ldots, M-1$, $\Delta\omega = 2\pi/T \approx 0.4f$ is the minimum resolvable frequency (which is constrained by the $T \approx 2$ days duration of the drift), and M is now half the number of observations in the time domain. The negative ($\omega_- < 0$) and positive ($\omega_+ > 0$) angular frequencies of $\widehat{\mathrm{Fr}}(\omega_k)$ can then be used to calculate the clockwise and counterclockwise components of the Froude number spectrum $\widehat{\mathrm{Fr}}^2_{\mathrm{CW}}(\omega_-)$ and $\widehat{\mathrm{Fr}}^2_{\mathrm{CCW}}(\omega_+)$, respectively. The spectra are normalized by $2\pi T$ so that

$$\overline{\mathrm{Fr}^2(t)} = \frac{\Delta t}{T}\sum_{n=0}^{2M-1}\frac{\frac{\partial u_a(t_n)}{\partial z}^2 + \frac{\partial v_a(t_n)}{\partial z}^2}{\overline{N}^2} \approx \Delta\omega\sum_{k=-M}^{M-1}\widehat{\mathrm{Fr}}^2(\omega_k), \tag{7}$$

and the contribution from different frequencies ω_k to the time-averaged $\overline{\mathrm{Fr}^2(t)}$ can be estimated by summing over a subset of the resolved frequencies ω_k. Figure 7 shows the Froude number frequency spectra averaged between $z = -41$ and -189 m. Confidence intervals for this depth-averaged spectrum are derived from a χ^2

distribution. The effective number of independent observations used to calculate the confidence intervals (five in this case) is estimated by dividing the depth over which the spectra were calculated by the largest integral depth scale calculated from the spatial correlation function of $\widehat{\mathrm{Fr}}^2(\omega_k, z)$.

These estimates of the CW and CCW components of $\widehat{\mathrm{Fr}}^2(\omega)$ in Fig. 7 reveal increased variance at frequencies $1.7f \gtrsim \omega \gtrsim f$ just above the Coriolis frequency. At these frequencies, almost all of the variance is in the CW rotary component, which explains about a quarter of the total Froude variance (CW + CCW) averaged from −41- to −189-m depth (Fig. 7b). The maximum in the Froude number spectrum is at $\omega_k = 1.2f$, which represents frequencies $1.4f \gtrsim \omega \gtrsim f$ and explains about 40% of the variance in the depth range $-40 > z > -80$ m (not shown). Depending on the depth, the two frequency bins ω_k with the largest variance, which represent frequencies $1.7f \gtrsim \omega \gtrsim f$, represent between 10% and 60% of the total Froude variance $\overline{\mathrm{Fr}^2}(t)$ (which ranges between about 0.1 and 0.5 here; see Fig. 8). At depths shallower than $z \approx -100$ m, the frequencies $1.7f \gtrsim \omega \gtrsim f$ contain approximately 50% of the total Froude variance. In this part of the water column, the two frequency bins ω_k with the largest variance, $1.7f \gtrsim \omega \gtrsim f$, are dominated by clockwise rotary motions as quantified by the rotary coefficient

$$\frac{\widehat{\mathrm{Fr}}^2_{\mathrm{CW}} - \widehat{\mathrm{Fr}}^2_{\mathrm{CCW}}}{\widehat{\mathrm{Fr}}^2_{\mathrm{CW}} + \widehat{\mathrm{Fr}}^2_{\mathrm{CCW}}} \tag{8}$$

(e.g., Gonella 1972), which exceeds a value of 0.8 (Fig. 8, right panel).

Together, the analysis of this and the previous section support the hypothesis that a large fraction of the total shear variance observed during this roughly 2-day Lagrangian survey of the Gulf Stream Front is associated with coherent NIWs. In particular, the shear vector is polarized so that it rotates clockwise with both increasing depth and increasing time on average, and at some depths the total shear variance is dominated by a narrow band of superinertial frequencies $1.7f \gtrsim \omega \gtrsim f$.

4. Comparison to theory of NIWs in submesoscale fronts

Given that a large fraction of the shear variance is apparently explained by NIWs, we use the dispersion and polarization relations for NIWs in a submesoscale front, as defined in Whitt and Thomas (2013), to assess the consistency between the observed spatial variability of the shear, the observed temporal variability of the shear, and the theory for NIWs in submesoscale fronts with $\mathrm{Ro} \sim \mathrm{Ri} \sim 1$. This theory makes several assumptions about the waves and the balanced flow, namely, that the NIWs are hydrostatic and low-amplitude relative to the geostrophic flow (i.e., a linear perturbation) and uniform in the alongfront direction and that the balanced flow is steady, geostrophic, and uniform in the alongfront direction as well (Whitt and Thomas 2013). In addition, the use of a dispersion relation implies an assumption that the properties of the wave field (such as wavelength and frequency) and balanced flow are slowly varying in space and time (e.g., Lighthill 1978). Hence, the theory is expected to be accurate in a submesoscale front like the North Wall of the Gulf Stream to the extent that these assumptions about the waves and balanced flow are reasonable. In this case, the theoretical results should be interpreted with some caution because the NIW shear is approximately comparable in magnitude to the balanced shear (see section 3a). The degree of symmetry in the alongfront direction is difficult to assess from this nearly Lagrangian dataset, but the balanced flow is clearly not a perfectly axi-symmetric jet (Fig. 1a). Finally, the medium (i.e., the balanced flow) varies relatively rapidly on the scales of the waves in both space and time. Despite the caveats, we proceed to analyze the observations using this theory.

In particular, looking in the cross-front plane we can estimate the angle that bands of ageostrophic shear $\partial \mathbf{u}_a/\partial z$ make with the horizontal and use it as an estimate for the slope of lines of constant wave phase (or constant wave shear), $s_{\mathrm{shear}} = -\alpha$, in the cross-front plane. Then the dispersion relation

$$\omega = \sqrt{f_{\mathrm{eff}}^2 + 2S^2\alpha + N^2\alpha^2}\,, \tag{9}$$

where $S^2 = f\partial u_g/\partial z$, $\alpha = l/m$, and $\mathbf{k} = (0, l, m)$ is the wave vector, can be used to infer the wave frequency from α and the properties of the background flow. The dispersion relation [(9)] reaches a minimum [defined in (1)] when wave phase lines align with isopycnals, that is, $s_{\mathrm{shear}} = -\alpha = S^2/N^2 = s_b$. This dispersion relation [(9)] is derived in the hydrostatic form used here by Whitt and Thomas (2013) and in nonhydrostatic form by Mooers (1975). See also Mooers (1970) and Whitt (2015) for further discussion of the theory and its applications.

To use this theory, the ageostrophic waves and geostrophic-balanced flow must be decomposed. The cross-stream shear $\partial v/\partial z$ is assumed to be entirely ageostrophic, while the streamwise shear $\partial u/\partial z$ can contain both balanced and unbalanced components. The method for isolating the geostrophic shear in the streamwise direction $\partial u_g/\partial z$ is described in the appendix.

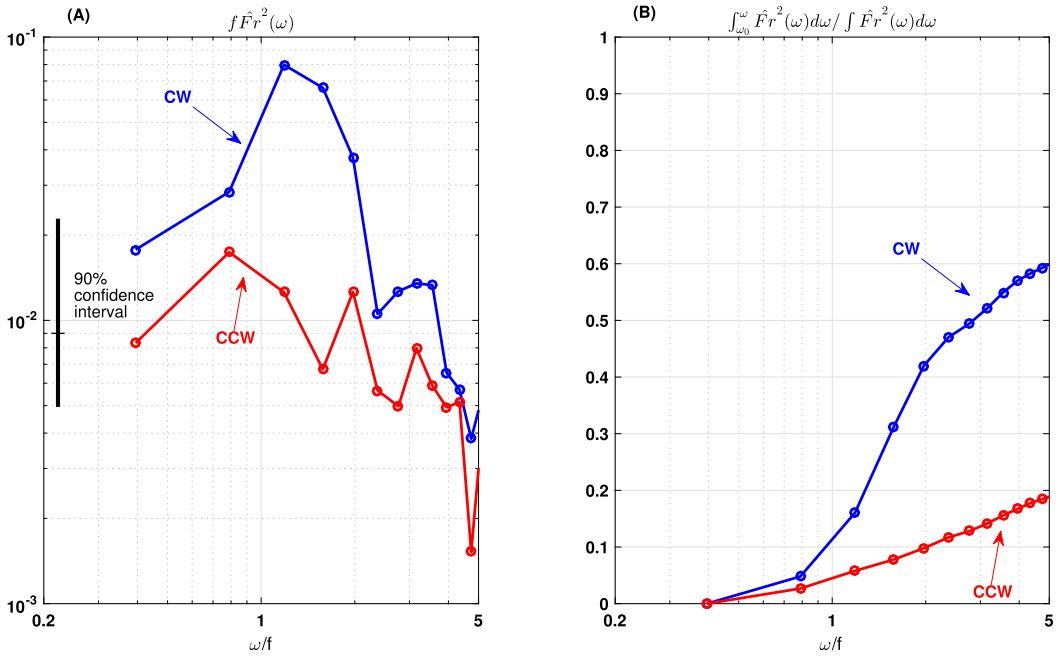

FIG. 7. (a) The depth average (from $z = -41$ to -189 m) of the CW and CCW rotary components of the Froude number spectrum $\widehat{\mathrm{Fr}}^2(\omega)$ as a function of the angular frequency ω. The 90% confidence interval is shown in black. (b) The cumulative fraction of the total variance associated with each frequency/rotary component; each component in (b) is normalized by the total Froude variance (CW + CCW); hence, the sum of the two components approaches one at high frequencies. Only the data shown in Fig. 4 are used in the calculation hence this average represents data within 350 m of the float path. The frequencies shown range from about 1/5 to 5 times the local Coriolis frequency, that is, periods of about 4 days to 4 h.

In an effort to obtain a precise estimate for $s_{\mathrm{shear}} = -\alpha$ from the observed shear, an algorithm was developed to identify the cross-front and vertical coordinates of large simply connected regions of ageostrophic shear bounded by contours of constant shear and compute their principal components, from which $s_{\mathrm{shear}} = -\alpha$ is derived. The procedure is outlined in the appendix and is performed in a region from $z = -30$ m to -170 m depth in each *Knorr* cross section from the drift (see Fig. 1a). A histogram of the measurements of s_{shear} determined via this method is shown in Fig. 9a along with a histogram of the isopycnal slope s_b (Fig. 9b). The ratio of s_{shear} to s_b in Fig. 9c shows that on average the most coherent shear structures are nearly parallel to or just slightly steeper than isopycnals.

From these observations of s_{shear}, the average wave frequency inferred from the dispersion relation (9) is $\omega = (1.11 \pm 0.14)f$, where $1.11f$ is the sample mean and $0.14f$ is the sample standard deviation of all the frequency estimates inferred via this method. The histogram of all the frequency estimates obtained from the dispersion relation is shown in Fig. 9d. This estimate of the dominant wave frequency derived from the dispersion relation (9) is consistent with the dominant frequency measured in the spectral analysis of section 3c, where the frequency bin $\omega_k = 1.2f$ has the highest amplitude (see Fig. 7). This frequency bin represents the frequency range $1.4f \gtrsim \omega \gtrsim f$; the width of the bin is set by the duration of the drift, which sets the spectral resolution $2\pi/T \approx \Delta\omega \approx 0.4f$ (see section 3). Differences between the two estimates of the frequency could also be attributable to spatial variability since the frequency spectra were calculated within 350 m of the float track, while the evaluation of the dispersion relation was made across entire cross-stream sections.

The theory of Whitt and Thomas (2013) also derives the polarization relations for NIWs and predicts how they change with the properties of a front. For plane waves, the polarization relations set the ratio of the energy in the clockwise to counterclockwise rotary components of velocity, which can be compared to the observational estimates based on the frequency spectra. Whitt and Thomas (2013) demonstrated that a plane wave with streamwise and cross-stream velocities $u_w = \Re\{\hat{u}\exp[i(ly + mz - \omega t)]\}$ and $v_w = \Re\{\hat{v}\exp[i(ly + mz - \omega t)]\}$ has a polarization

$$\hat{u} = \frac{i\hat{v}}{\omega f}(f_{\mathrm{eff}}^2 + \alpha S^2). \tag{10}$$

Here, we use this result to derive a theoretical expression for the rotary coefficient (8), which can be written in a variety of ways, for example,

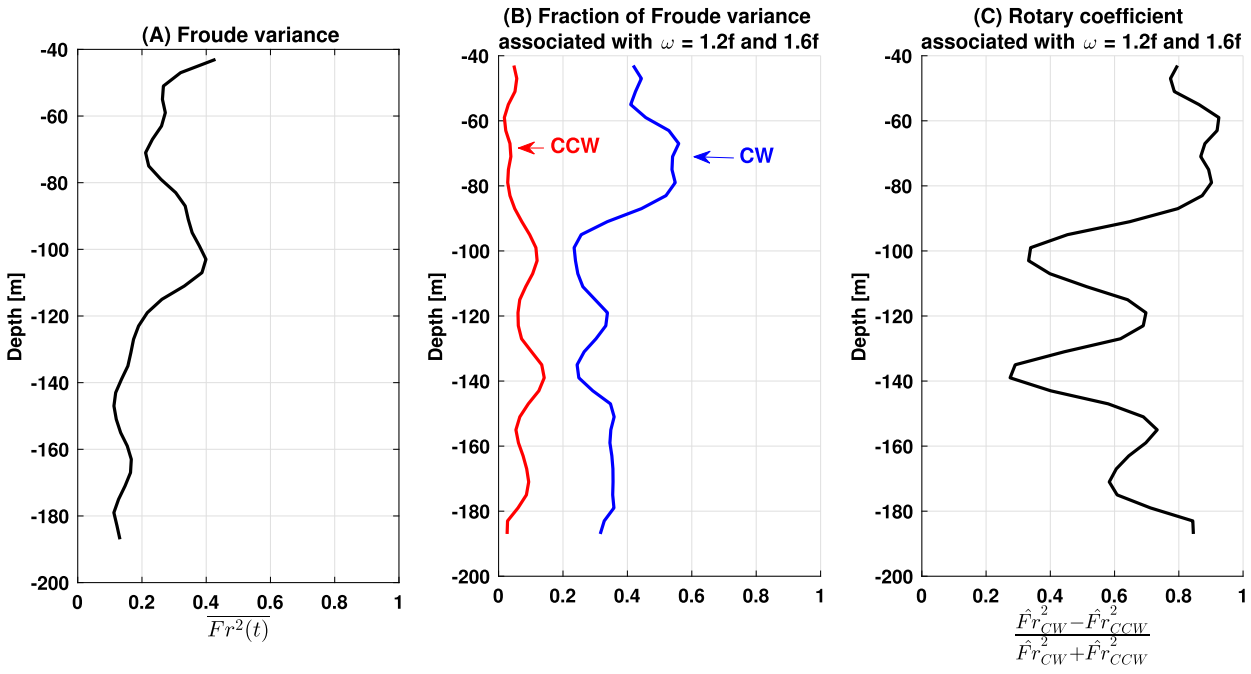

FIG. 8. (a) The average Froude number variance within 350 m of the float path $\overline{\mathrm{Fr}^2(t)}$ at each depth z_n; (b) the fraction of the total Froude variance associated with the CW and CCW components of the two highest-amplitude components of $\widehat{\mathrm{Fr}}^2_{\mathrm{CW}}(\omega)$, that is $\mathrm{CW} = \Delta\omega\sum_{k=3,4}\widehat{\mathrm{Fr}}^2(-\omega_k)$, $\mathrm{CCW} = \Delta\omega\sum_{k=3,4}\widehat{\mathrm{Fr}}^2(\omega_k)$, $\omega_3 = 1.2f$ and $\omega_4 = 1.6f$; and (c) their rotary coefficient [(8)].

$$\frac{(\widehat{\mathrm{Fr}}^2_{\mathrm{CW}} - \widehat{\mathrm{Fr}}^2_{\mathrm{CCW}})}{(\widehat{\mathrm{Fr}}^2_{\mathrm{CW}} + \widehat{\mathrm{Fr}}^2_{\mathrm{CCW}})} = \frac{(\widehat{\mathrm{KE}}_{\mathrm{CW}} - \widehat{\mathrm{KE}}_{\mathrm{CCW}})}{(\widehat{\mathrm{KE}}_{\mathrm{CW}} + \widehat{\mathrm{KE}}_{\mathrm{CCW}})}) = \frac{|u_-|^2 - |u_+|^2}{|u_-|^2 + |u_+|^2} = \frac{(f^2_{\mathrm{eff}} + \alpha S^2 + \omega f)^2 - (f^2_{\mathrm{eff}} + \alpha S^2 - \omega f)^2}{(f^2_{\mathrm{eff}} + \alpha S^2 + \omega f)^2 + (f^2_{\mathrm{eff}} + \alpha S^2 - \omega f)^2} = \frac{2(f^2_{\mathrm{eff}} + \alpha S^2)\omega f}{(f^2_{\mathrm{eff}} + \alpha S^2)^2 + \omega^2 f^2}, \tag{11}$$

where

$$u_+ = \frac{1}{2}\{[\Re(\hat{u}) + \Im(\hat{v})] + i[\Re(\hat{v}) - \Im(\hat{u})]\}, \quad \text{and}$$

$$u_- = \frac{1}{2}\{[\Re(\hat{u}) - \Im(\hat{v})] + i[\Re(\hat{v}) + \Im(\hat{u})]\}.$$

In the limit that $\alpha \to 0$ and $f_{\mathrm{eff}} \to f$, then (11) reduces to the rotary coefficient derived by Gonella (1972), that is, $2f\omega/(f^2 + \omega^2)$. The inferred frequency from the dispersion relation, slope of the ageostrophic shear $s_{\mathrm{shear}} = -\alpha$, and vorticity and baroclinicity of the front were used to calculate (11), a histogram of which is shown in Fig. 9e. The theory predicts that the kinetic energy of the NIW is primarily in clockwise rotary motions, consistent with the findings from the frequency spectra (cf. Fig. 8).

5. Discussion

a. *Wave propagation, trapping, and amplification*

Motivated by the consistency between the measured properties of the NIWs and the predictions of Whitt and Thomas (2013), we apply the theory to explore the propagation, trapping, and amplification of NIWs in the density and vorticity fields observed during the drift. In particular, we ask the following questions:

(i) How might superinertial NIWs with the observed dominant frequencies and wavenumbers propagate in the spatially variable medium of the Gulf Stream Front (e.g., Fig. 2)?
(ii) Why might superinertial NIWs have the highest amplitude in the North Wall of the Gulf Stream?

We start with the second question. As shown in Fig. 2, the North Wall of the Gulf Stream is characterized by order-one Ro and Ri. As a result, the minimum frequency $\omega_{\mathrm{min}} = f\sqrt{1 + \mathrm{Ro} - \mathrm{Ri}^{-1}}$ is substantially different from f, as shown in Fig. 10a. In particular, below the mixed layer ω_{min} is greater than the local Coriolis frequency in most of the region of interest (see Fig. 10a). Hence, theory suggests that propagating subinertial waves cannot exist here, which may explain why the peak in the observed frequency spectrum (which was calculated near the float at $y \approx 0$ for depths between -41 and -189 m; Fig. 7) does not surround f but is

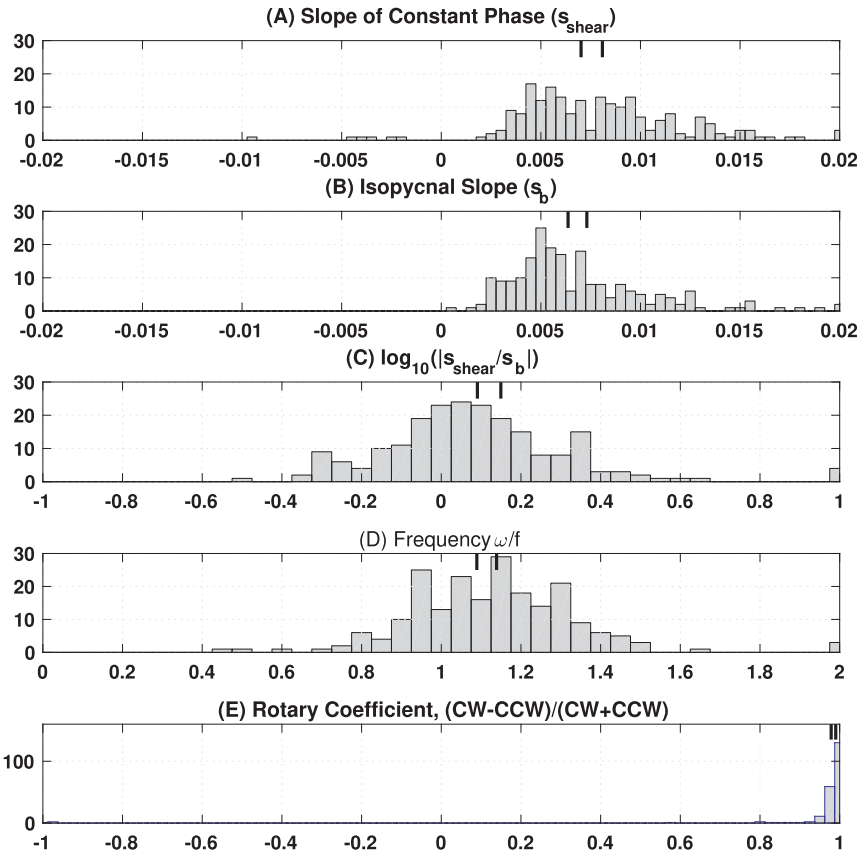

FIG. 9. Histograms of the (a) inferred slope of constant wave shear $s_{\text{shear}} = -\alpha$, (b) isopycnal slope s_b, (c) logarithm of the ratio s_{shear}/s_b, (d) inferred frequencies obtained using $s_{\text{shear}} = -\alpha$ and the dispersion relation [(9)], and (e) rotary coefficient [(11)]. Bootstrap 95% confidence intervals for the arithmetic mean of each histogram are indicated by black hash marks. The histograms were calculated data from 30 to 170 m below the surface along the track of the R/V *Knorr* (i.e., not merely those data within 350 m of the float).

instead centered around somewhat higher superinertial frequencies.

We can better quantify the propagation of the NIWs using ray tracing, namely, by solving for the position $\mathbf{r}_w$ that wave packets trace with time

$$\frac{d\mathbf{r}_w}{dt} \equiv \mathbf{c}_g, \tag{12}$$

where

$$\mathbf{c}_g \equiv \nabla_{(l,m)}\omega = \frac{(S^2 + N^2\alpha)}{\omega m}(1, -\alpha) \tag{13}$$

is the group velocity of NIWs in a front (Whitt and Thomas 2013). Note, however, that the usual assumption of a slowly varying wave train, which is required for ray tracing to be valid, does not hold here because the medium varies rapidly on the spatial and temporal scales of the waves. On the one hand, slow spatial variations are not strictly required to characterize the propagation of the wave energy across the front in the theory of Whitt and Thomas (2013). In particular, ray paths parallel characteristics of the governing partial differential equation [(14) in Whitt and Thomas (2013)], and these characteristics accurately characterize the two-way propagation direction of wave energy even in a medium that varies on short spatial scales, as demonstrated by Whitt and Thomas (2013; see also Mooers 1975; Bühler and Holmes-Cerfon 2011). On the other hand, the potential for temporal variability in the medium on the time scale of the waves poses a number of challenging problems. Therefore, the conclusions derived from the ray tracing should be viewed with caution in this context.

Ray paths of wave packets with frequency $\omega = 1.13f$ (a value close to the mean in the histogram of the dispersion relation; e.g., Fig. 9d) initiated at a depth of 70 m and cross-stream locations $y = -5$ and $+6$ km were calculated for the *Atlantis* section shown in Fig. 2. Two rays are calculated for each location,

corresponding to wave propagation on the two wave characteristics with slopes

$$s_c = s_b \pm \sqrt{\frac{\omega^2 - \omega_{\min}^2}{N^2}}. \tag{14}$$

The frequency $\omega = 1.13f$ is close to f_{eff} at the initial locations of the wave packets, and consequently the shallow characteristic in (14), that is, the negative root, is nearly horizontal, while the steep characteristic is close to twice the isopycnal slope, as is evident in the shape of the ray paths near their origin (Fig. 10b). The waves can only propagate in regions where the minimum frequency is less than their frequency. When the waves encounter locations where $\omega = \omega_{\min}$ (i.e., the locus of turning points that define separatrix bounding regions where the wave equation transitions from being hyperbolic to elliptic) they reflect and move along the opposite characteristic from which they traveled. The spatial structure of the separatrix for these superinertial waves is largely determined by the strong cyclonic vorticity in the North Wall of the Gulf Stream (cf. Fig. 2b and Fig. 10a), which is broken into filaments by flow instabilities (Klymak et al. 2016). The fragmentation of the separatrix can lead to wave trapping with rays experiencing multiple reflections between vortex filaments (e.g., Fig. 10b; between −5 and 0 km and 0 and 10 km).

While trapping could lead to amplification of the superinertial waves, wave shoaling could play a role as well. The magnitude of the group velocity [defined in (13)] varies significantly along ray paths (Fig. 10b) and at the separatrix the magnitude of the group velocity equals zero since $\omega = \omega_{\min}$ and $\alpha = -s_b$. Consequently, as wave packets approach the separatrix their energy density should increase to conserve the energy flux, namely, the waves shoal. If the separatrix aligns with the tilted isopycnals of a front, then the reflected ray cannot escape from the separatrix and a slantwise critical layer forms, leading to especially intense wave shear (Whitt and Thomas 2013). There are several locations in the *Atlantis* section where this criterion is nearly met for $\omega = 1.13f$, for example, $y \approx 2$ km and $z \approx -80$ m and $y \approx 10$ km and $z \approx -175$ m (Fig. 10b). Hence, it is plausible that superinertial NIWs can be trapped and amplified in the North Wall of the Gulf Stream, which could explain the observed superinertial peak in the Froude variance associated with downward-propagating NIWs.

b. Superinertial wave generation

How could these downward-propagating superinertial NIWs have been generated? The most obvious source of energy for the NIWs is the time-variable winds (e.g., Fig. 4a). In a geostrophic current with vertical vorticity, winds can accelerate oscillatory motions in the surface mixed layer with frequencies that depart from the inertial frequency because the resonant forcing frequency in such a current is $f_{\text{eff}} = f\sqrt{1 + \zeta/f}$, not f (e.g., Weller 1982). Since vorticity in the North Wall of the Gulf Stream is cyclonic, this resonant frequency exceeds f, suggesting that wind-driven oscillations in the surface mixed layer should be superinertial and hence could excite NIWs of similar frequency. To test this hypothesis we numerically integrate the "slab mixed layer" momentum equations modified to account for the effects of vorticity (e.g., Weller 1982; Klein and Hua 1988; Whitt and Thomas 2015):

$$\frac{dU}{dt} - (f + \overline{\zeta}^z)V = \frac{\tau_w^x}{\rho_o H} - \gamma U, \quad \text{and} \tag{15}$$

$$\frac{dV}{dt} + fU = \frac{\tau_w^y}{\rho_o H} - \gamma V, \tag{16}$$

where (U, V) is the velocity averaged over the mixed layer of depth H, $\overline{\zeta}^z$ is the depth-averaged vorticity of the geostrophic flow, $\gamma = 10^{-5}\,\text{s}^{-1}$ is a damping coefficient that parameterizes wave radiation and local dissipation, and (τ_w^x, τ_w^y) is a time series of the observed winds. The initial condition is $U = V = 0$, and the simulation begins at yearday 59.5. For the calculation, we use a mixed layer depth $H = 50$ m and the vertical vorticity of the Gulf Stream averaged within 350 m of the float $\overline{\zeta}^z = 0.4f$, which yields an effective Coriolis frequency $f_{\text{eff}} = 1.18f$. The solution for the inertial components, $U_I = U - U_E$ and $V_I = V - V_E$, is plotted in Fig. 11 along with its rotary frequency spectrum (calculated using the method outlined in section 3c). Here, the steady Ekman solution, that is

$$U_E = \frac{\tau_w^y}{\rho_o H f}, \quad \text{and} \tag{17}$$

$$V_E = -\frac{\tau_w^x}{\rho_o H(f + \overline{\zeta}^z)}, \tag{18}$$

is subtracted to isolate the oscillating inertial part of the solution (MATLAB code to solve the slab mixed layer model is available at https://github.com/danielwhitt/slabML).

The calculation supports the hypothesis that the local wind stress could have excited the observed NIWs. In particular, the modeled mixed layer inertial currents exhibit speeds ranging from 0.05 and 0.1 m s^{-1}, consistent with the observed shear, which has a velocity scale of $(1/m)(\partial|\mathbf{u}|/\partial z) \sim 0.1\,\text{m s}^{-1}$. Moreover, like the observed shear, the modeled mixed layer velocities are dominated by clockwise rotation at slightly superinertial

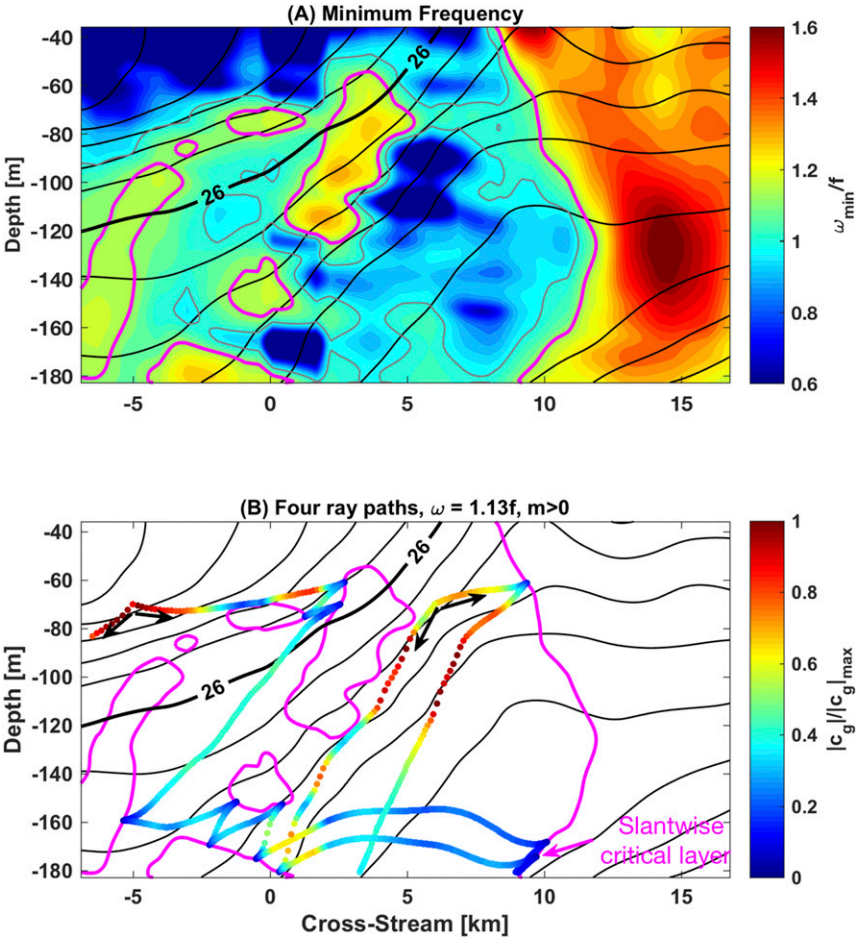

FIG. 10. (a) The minimum frequency of inertial gravity waves in a front [defined in (1)] for the *Atlantis* section shown in Fig. 2. (b) Four example ray paths for a wave with frequency $\omega = 1.13f$ and a positive vertical wavenumber $m > 0$. The magnitude of the group velocity normalized by its maximum value on a ray is indicated in color in (b). The contours of constant $\omega_{\min}$ are in some places nearly parallel to isopycnals, which is the characteristic signature of a slantwise critical layer where the group velocity goes to zero and ray paths cannot escape. Magenta contours in both panels indicate where $\omega_{\min} = 1.13f$ and the gray contours in (a) indicate where $\omega_{\min} = f$.

frequencies and present a similarly shaped spectrum (cf. Figs. 7 and 11b). In addition, it is worth noting that this slab mixed layer model also predicts that wind-generated, near-inertial oscillations in the ocean mixed layer become incoherent across the front over a time scale of order $1/f$ because of the order-one cross-front variations in $\overline{\zeta}/f$ at the Gulf Stream (see Fig. 2b). These large variations in $\overline{\zeta}/f$ can, therefore, facilitate the downward radiation of near-inertial wave energy between the vorticity filaments at the North Wall via a submesoscale inertial chimney effect (van Meurs 1998; Lee and Niiler 1998; Whitt and Thomas 2015; Whitt 2015). Although we have some ADCP data from outside the front during the LatMix experiment, which suggests that the CW and CCW components of $\widehat{\mathrm{Fr}}^2$ are generally about equal there (as in Garrett and Munk 1972), these data are not exactly coincident in time with this survey. Hence, we do not have the data to prove that the observed asymmetry between CW and CCW Froude variance is unique to the North Wall during the survey.

6. Comparison with other observations

The observations presented here are unique in that we are observing the temporal evolution of near-inertial shear in a submesoscale front in a nearly Lagrangian frame of reference with a spatial resolution of $O(1)$ km and a temporal resolution of $O(10)$ min. That said, our results are

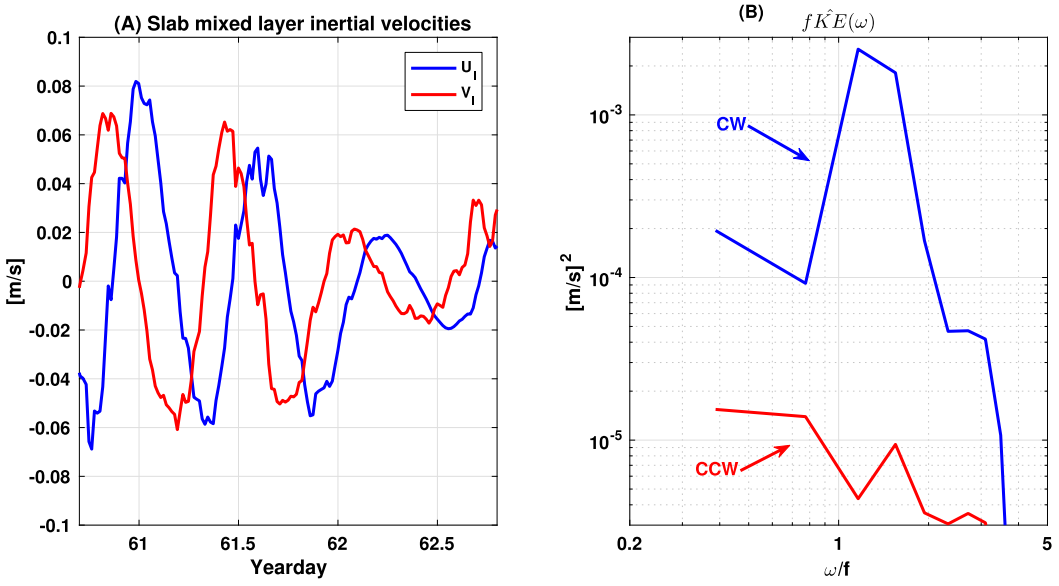

FIG. 11. (a) Time series of mixed layer near-inertial velocities calculated using the slab mixed layer model, as described in section 5b. (b) CW and CCW components of the rotary kinetic energy spectrum associated with the time series in (a).

qualitatively similar to a variety of earlier observations of banded, near-inertial shear interacting with mesoscale and submesoscale flow features. In this section, we will briefly describe some of the previously published observations of NIWs and discuss how those observations compare to the observations of NIWs discussed here.

For example, the shear bands (e.g., Figs. 3, 4) appear qualitatively similar to observations of near-inertial waves trapped in anticyclonic warm-core rings (e.g., Kunze 1986; Kunze et al. 1995; Jaimes and Shay 2010; Joyce et al. 2013), although the geometry is different. Whereas the shear features may have been confined in three dimensions inside the anticyclonic rings, the evidence here suggests that the amplified shear features in the North Wall are rather two-dimensional, confined in the cross-front and vertical directions but not along the front. Furthermore, Kunze et al. (1995) observed enhanced energy dissipation associated with near-inertial shear in the center of a warm-core ring but not on the edges. Our observations, on the other hand, exhibit strong near-inertial shear at the north edge of the Gulf Stream in the same location as the strongest lateral density gradients and strong cyclonic vertical vorticity (see Fig. 2). Our observations further contrast with those in rings because the observed frequency is superinertial here (Fig. 7), whereas it is generally assumed [or—more rarely—observed, as in Perkins (1976) and Jaimes and Shay (2010)] to be subinertial in anticyclonic rings.

Several studies have also observed elevated near-inertial wave energy in mesoscale and submesoscale fronts. For example, Rainville and Pinkel (2004) observed elevated shear variance and coherent structures characteristic of near-inertial waves blocked by the strong vertical vorticity and high effective Coriolis frequency f_{eff} in the Kuroshio. D'Asaro et al. (2011) observed banded shear in a strong submesoscale front in the Kuroshio and hypothesized that the shear was associated with near-inertial waves, although the wave dynamics were not explored in detail. Kunze and Sanford (1984) and Alford et al. (2013) observed strong, coherent, banded, near-inertial shear modulated by the Pacific Subtropical Front, where $\text{Ro} \sim \text{Ri}^{-1} \sim 0.1$. Pallàs-Sanz et al. (2016) observed trapped near-inertial waves at a critical layer at the base of the Loop Current after a hurricane. Mied et al. (1987) observed a near-inertial wave packet where an eddy impinged on a mesoscale frontal jet in the North Atlantic subtropical zone. The wave packet was confined to a 25-km-wide region in the front and was associated with coherent patches of elevated temperature variance (Marmorino et al. 1987; Marmorino 1987) and superinertial frequencies, similar to our observations. Whitt and Thomas (2013) observed banded shear in a ~200-km-wide section (with ~10-km resolution) across the winter Gulf Stream and noted that the properties of the shear were consistent with the spatial structure of a subinertial wave at a slantwise critical layer. Collocated shear microstructure profiles showed enhanced dissipation between 400 and 600 m in the upper thermocline in the same location as these

shear structures (Inoue et al. 2010), suggesting a link between the shear and enhanced turbulence. None of the above studies considered the possibility that superinertial waves may be trapped between filaments of cyclonic vertical vorticity, as discussed here.

7. Conclusions

A high-resolution Lagrangian survey of the North Wall of the Gulf Stream made during strong and variable wintertime atmospheric forcing provided the unique, new opportunity to observe the interaction of NIWs with a current in the submesoscale dynamical regime and dominated by cyclonic vorticity. The ageostrophic vertical shear inferred from the survey has features characteristic of coherent, downward-propagating NIWs. Namely, the shear is polarized in space and time, such that it rotates primarily clockwise with increasing depth and increasing time. Frequency spectra exhibit a distinct peak in the clockwise rotary component at frequencies $1.7f \gtrsim \omega \gtrsim f$ that are slightly higher than the Coriolis frequency. At some depths these clockwise frequencies explain more than 50% of the total shear variance measured over 2 days.

The high-resolution sections across the front allow us to check the consistency of the properties of the observed near-inertial shear with the theory of NIWs propagating perpendicular to strongly baroclinic currents (Mooers 1975; Whitt and Thomas 2013). In particular, we can estimate the aspect ratio of the observed banded shear structures and use it in the dispersion relation of Whitt and Thomas (2013), which is designed for near-inertial waves in a submesoscale front to obtain frequency estimates that are independent of the spectral analysis and contrast the results. The observed consistency between the two frequency estimates, both of which are superinertial, motivate an extension to the theoretical analysis of Whitt and Thomas (2013), which focuses on the properties and propagation of subinertial waves in submesoscale fronts, to explore how superinertial waves propagate in the North Wall of the Gulf Stream, where the vertical vorticity is strongly cyclonic and the minimum frequency for inertia–gravity waves is greater than the local Coriolis frequency. Ray tracing/characteristic paths suggest that the propagation of superinertial wave energy is strongly modified by narrow filaments of strong, cyclonic vertical vorticity in the North Wall of the Gulf Stream. Superinertial waves can bounce between the cyclonic filaments and become trapped and amplified at slantwise critical layers between these filaments, a scenario that has not been previously considered in the literature (see Fig. 10 for an illustration). In addition, a slab mixed layer model suggests that variable winds are a plausible local source of energy for the observed superinertial waves because they resonantly force superinertial motions, owing to the cyclonic vorticity of the current. The slab model also suggests that large cross-front variations in the cyclonic vertical vorticity cause mixed layer inertial oscillations to become incoherent on short time and space scales, facilitating more rapid downward propagation of wave energy between cyclonic vorticity filaments at the North Wall caused by a submesoscale inertial chimney effect. However, these theoretical results should be viewed with caution because some of the assumptions used to obtain the theoretical results are not met. In addition, we have not proved that other theories cannot explain the observations. For example, the balanced flow could also be a source of the observed downward-propagating internal wave energy (e.g., Danioux et al. 2012; Alford et al. 2013; Nagai et al. 2015; Barkan et al. 2017; Shakespeare and Hogg 2017), but quantifying the magnitude of the energy flux between the balanced flow and the waves is beyond the scope of this article. Nevertheless, the consistency between the proposed description of the physics and the observations is encouraging and motivates further efforts to better constrain the observations and to explore the theoretical physical scenario in a more realistic context using numerical simulations.

Although we have not explicitly explored the link between the NIWs observed here and microscale turbulence, a number of previously published studies have demonstrated that coherent downward-propagating NIWs may be associated with enhanced turbulence (e.g., Marmorino et al. 1987; Marmorino 1987; Hebert and Moum 1994; Kunze et al. 1995; Polzin et al. 1996; Alford and Gregg 2001; Inoue et al. 2010). These previously published observations show that coherent near-inertial waves can directly modify turbulence and that wave–mean flow interactions can facilitate the concentration, amplification, and ultimate decay of near-inertial waves via turbulent dissipation. The observations collected here show that a large fraction of the Froude variance is associated with downward-propagating NIWs in the North Wall of the Gulf Stream. The superposition of this wave shear with the thermal wind shear of the front results in banded regions of low Richardson number (e.g., Fig. 3c), which could be associated with enhanced turbulence. As turbulent mixing may be important for driving water mass transformation at the North Wall of the Gulf Stream (e.g., Klymak et al. 2016), coherent downward-propagating NIWs may also play an important role in water mass transformation in the upper pycnocline here. In addition, similar behavior could also occur at other western boundary currents, such as the Kuroshio, where

filaments of strong cyclonic vorticity and near-inertial waves are prominent features of the circulation (e.g., Nagai et al. 2009, 2012). However, future work will have to explore these hypotheses, which are beyond the scope of this article.

Acknowledgments. The data were obtained during the Scalable Lateral Mixing and Coherent Turbulence (LatMix) Department Research Initiative, funded by the United States Office of Naval Research. DBW and LNT were supported by ONR Grant N00014-09-1-0202 and NSF Grant OCE-1260312. DBW was also supported by an NSF postdoctoral fellowship OCE-1421125. JMK was supported by ONR Grant N00014-11-1-0165. EAD was supported by ONR Grant N00014-09-1-0172. CML was supported by ONR Grant N00014-09-1-0266. Data and visualization scripts are available from the lead author (dwhitt@ucar.edu). The authors thank the crew and officers of the R/V *Knorr* and R/V *Atlantis* as well as the rest of the LatMix 2012 science team and the staff of the Applied Physics Laboratory at the University of Washington for making this remarkable experiment possible. DBW would particularly like to thank Dave Winkel for his help with the processing of the shipboard ADCP data.

APPENDIX

Algorithm for Computing the Shear Aspect Ratio

To estimate the aspect ratio of the waves, $\alpha = l/m$, and infer their frequency from the dispersion relation [(9)], we use the following procedure:

(i) The coordinate system is rotated into a streamwise/cross-stream (x, y) coordinate system, as described in section 2. Then, the thermal wind shear

$$\frac{\partial u_g}{\partial z} = -\frac{1}{f}\frac{\partial b_g}{\partial y} \tag{A1}$$

is inferred in each section made by the R/V *Knorr* (e.g., Fig. 3) from the cross-stream buoyancy gradient, after additionally smoothing the density field ρ with a 40 m (vertical) by 7 km (lateral) averaging filter, that is, $b_g = -g\langle\rho\rangle/\rho_o$, where the brackets denote the filter, g is the gravitational acceleration, and ρ_o is a reference density. Then the streamwise ageostrophic shear $\partial u_a/\partial z$ is inferred in each section by subtracting this thermal wind shear from the observed shear. The cross-stream shear is assumed to be entirely ageostrophic, that is, $\partial v_a/\partial z = \partial v/\partial z$.

(ii) In each section, the two components of the ageostrophic shear as well as the y (cross stream) and z (vertical) coordinate grids are extracted and normalized by scaling so that the mean and variance of all four fields are zero and one, respectively.

(iii) In each section the set of simply connected regions with shear magnitude greater than a threshold magnitude is identified [each region is a set of (y, z) pairs]. The chosen threshold may depend on the distribution of the shear in a given section, but we used just one value for the observations (0.5 in normalized shear units).

(iv) One thousand bootstrap samples are created for each simply connected region.

(v) For each bootstrap sample, the slope of the first principle component of the set of (y, z) pairs was used as a value for $-\alpha$ (after rescaling y and z to physical units). The background flow parameters in (9), including f_{eff}^2, S^2, and N^2, were estimated using averages over the simply connected ageostrophic shear region for each coefficient.

(vi) If the 95% confidence interval for the bootstrap frequency estimates in a given region is narrower than $0.2f$, then the result is considered robust and the frequency estimate is retained in the histograms in Fig. 9.

REFERENCES

Alford, M., and R. Pinkel, 2000: Observations of overturning in the thermocline: The context of ocean mixing. *J. Phys. Oceanogr.*, **30**, 805–832, https://doi.org/10.1175/1520-0485(2000)030<0805:OOOITT>2.0.CO;2.

——, and M. Gregg, 2001: Near-inertial mixing: Modulation of shear, strain and microstructure at low latitude. *J. Geophys. Res.*, **106**, 16 947–16 968, https://doi.org/10.1029/2000JC000370.

——, A. Y. Shcherbina, and M. C. Gregg, 2013: Observations of near-inertial internal gravity waves radiating from a frontal jet. *J. Phys. Oceanogr.*, **43**, 1225–1239, https://doi.org/10.1175/JPO-D-12-0146.1.

Barkan, R., K. B. Winters, and J. C. McWilliams, 2017: Stimulated imbalance and the enhancement of eddy kinetic energy dissipation by internal waves. *J. Phys. Oceanogr.*, **47**, 181–198, https://doi.org/10.1175/JPO-D-16-0117.1.

Bühler, O., and M. W. McIntyre, 2005: Wave capture and wave–vortex duality. *J. Fluid Mech.*, **534**, 67–95, https://doi.org/10.1017/S0022112005004374.

——, and M. Holmes-Cerfon, 2011: Decay of an internal tide due to random topography in the ocean. *J. Fluid Mech.*, **678**, 271–293, https://doi.org/10.1017/jfm.2011.115.

Danioux, E., P. Klein, and P. Riviere, 2012: Spontaneous inertia-gravity-wave generation by surface-intensified turbulence. *J. Fluid Mech.*, **699**, 153–173, https://doi.org/10.1017/jfm.2012.90.

D'Asaro, E. A., 2003: Performance of autonomous Lagrangian floats. *J. Atmos. Oceanic Technol.*, **20**, 896–911, https://doi.org/10.1175/1520-0426(2003)020<0896:POALF>2.0.CO;2.

——, and H. Perkins, 1984: A near-inertial internal wave spectrum for the Sargasso Sea in late summer. *J. Phys. Oceanogr.*, **14**,

489–505, https://doi.org/10.1175/1520-0485(1984)014<0489:ANIIWS>2.0.CO;2.

——, C. Lee, L. Rainville, R. Harcourt, and L. Thomas, 2011: Enhanced turbulence and energy dissipation at ocean fronts. *Science*, **332**, 318–322, https://doi.org/10.1126/science.1201515.

Emery, W. J., and R. E. Thomson, 2001: *Data Analysis Methods in Physical Oceanography*. 2nd ed. Elsevier, 638 pp.

Garrett, C., and W. Munk, 1972: Space-time scales of internal waves. *Geophys. Fluid Dyn.*, **3**, 225–264, https://doi.org/10.1080/03091927208236082.

Gonella, J., 1972: A rotary-component method for analysing meteorological and oceanographic vector time series. *Deep-Sea Res. Oceanogr. Abstr.*, **19**, 833–846, https://doi.org/10.1016/0011-7471(72)90002-2.

Hebert, D., and J. Moum, 1994: Decay of a near-inertial wave. *J. Phys. Oceanogr.*, **24**, 2334–2351, https://doi.org/10.1175/1520-0485(1994)024<2334:DOANIW>2.0.CO;2.

Inoue, R., M. C. Gregg, and R. R. Harcourt, 2010: Mixing rates across the Gulf Stream, part 1: On the formation of Eighteen Degree Water. *J. Mar. Res.*, **68**, 643–671, https://doi.org/10.1357/002224011795977662.

Jaimes, B., and L. K. Shay, 2010: Near-inertial wave wake of Hurricanes Katrina and Rita over mesoscale oceanic eddies. *J. Phys. Oceanogr.*, **40**, 1320–1337, https://doi.org/10.1175/2010JPO4309.1.

Joyce, T., J. Toole, P. Klein, and L. Thomas, 2013: A near-inertial mode observed within a Gulf Stream warm-core ring. *J. Geophys. Res. Oceans*, **118**, 1797–1806, https://doi.org/10.1002/jgrc.20141.

Klein, P., and B. L. Hua, 1988: Mesoscale heterogeneity of the wind-driven mixed layer: Influence of a quasigeostrophic flow. *J. Mar. Res.*, **46**, 495–525, https://doi.org/10.1357/002224088785113568.

Klymak, J. M., and Coauthors, 2016: Submesoscale streamers exchange water on the North Wall of the Gulf Stream. *Geophys. Res. Lett.*, **43**, 1226–1233, https://doi.org/10.1002/2015GL067152.

Kunze, E., 1985: Near-inertial wave propagation in geostrophic shear. *J. Phys. Oceanogr.*, **15**, 544–565, https://doi.org/10.1175/1520-0485(1985)015<0544:NIWPIG>2.0.CO;2.

——, 1986: The mean and near-inertial velocity fields in a warm-core ring. *J. Phys. Oceanogr.*, **16**, 1444–1461, https://doi.org/10.1175/1520-0485(1986)016<1444:TMANIV>2.0.CO;2.

——, and T. Sanford, 1984: Observations of near-inertial waves in a front. *J. Phys. Oceanogr.*, **14**, 566–581, https://doi.org/10.1175/1520-0485(1984)014<0566:OONIWI>2.0.CO;2.

——, R. W. Schmidt, and J. M. Toole, 1995: The energy balance in a warm-core ring's near-inertial critical layer. *J. Phys. Oceanogr.*, **25**, 942–957, https://doi.org/10.1175/1520-0485(1995)025<0942:TEBIAW>2.0.CO;2.

Large, W., and S. Pond, 1981: Open ocean momentum flux measurements in moderate to strong winds. *J. Phys. Oceanogr.*, **11**, 324–336, https://doi.org/10.1175/1520-0485(1981)011<0324:OOMFMI>2.0.CO;2.

Leaman, K., and T. Sanford, 1975: Vertical energy propagation of inertial waves: A vector spectral analysis of velocity profiles. *J. Geophys. Res.*, **80**, 1975–1978, https://doi.org/10.1029/JC080i015p01975.

Lee, D., and P. Niiler, 1998: The inertial chimney: The near-inertial energy drainage from the ocean surface to the deep layer. *J. Geophys. Res.*, **103**, 7579–7591, https://doi.org/10.1029/97JC03200.

Lighthill, J., 1978: *Waves in Fluids*. Cambridge University Press, 504 pp.

Lomb, N. R., 1976: Least-squares frequency analysis of unequally spaced data. *Astrophys. Space Sci.*, **39**, 447–462, https://doi.org/10.1007/BF00648343.

Marmorino, G., 1987: Observations of small-scale mixing processes in the seasonal thermocline. Part II: Wave breaking. *J. Phys. Oceanogr.*, **17**, 1348–1355, https://doi.org/10.1175/1520-0485(1987)017<1348:OOSSMP>2.0.CO;2.

——, L. Rosenblum, and C. Trump, 1987: Fine-scale temperature variability: The influence of near-inertial waves. *J. Geophys. Res.*, **92**, 13 049–13 062, https://doi.org/10.1029/JC092iC12p13049.

Mied, R. P., G. J. Lindemann, and C. Trump, 1987: Inertial wave dynamics in the North Atlantic subtropical zone. *J. Geophys. Res.*, **92**, 13 063–13 074, https://doi.org/10.1029/JC092iC12p13063.

Mooers, C. N. K., 1970: The interaction of an internal tide with the frontal zone in a coastal upwelling region. Ph.D. thesis, Oregon State University, 480 pp.

——, 1975: Several effects of a baroclinic current on the cross-stream propagation of inertial-internal waves. *Geophys. Fluid Dyn.*, **6**, 245–275, https://doi.org/10.1080/03091927509365797.

Munk, W., 1981: Internal waves and small-scale processes. *Evolution of Physical Oceanography*, B. A. Warren and C. Wunsch, Eds., MIT Press, 264–291.

Nagai, T., A. Tandon, H. Yamazaki, and M. J. Doubell, 2009: Evidence of enhanced turbulent dissipation in the frontogenetic Kuroshio Front thermocline. *Geophys. Res. Lett.*, **36**, L12609, https://doi.org/10.1029/2009GL038832.

——, ——, ——, ——, and S. Gallager, 2012: Direct observations of microscale turbulence and thermohaline structure in the Kuroshio Front. *J. Geophys. Res.*, **117**, C08013, https://doi.org/10.1029/2011JC007228.

——, ——, E. Kunze, and A. Mahadevan, 2015: Spontaneous generation of near-inertial waves by the Kuroshio Front. *J. Phys. Oceanogr.*, **45**, 2381–2406, https://doi.org/10.1175/JPO-D-14-0086.1.

Pallàs-Sanz, E., J. Candela, J. Sheinbaum, J. Ochoa, and J. Jouanno, 2016: Trapping of the near-inertial wave wakes of two consecutive hurricanes in the Loop Current. *J. Geophys. Res. Oceans*, **121**, 7431–7454, https://doi.org/10.1002/2015JC011592.

Perkins, H., 1976: Observed effect of an eddy on inertial oscillations. *Deep-Sea Res. Oceanogr. Abstr.*, **23**, 1037–1042, https://doi.org/10.1016/0011-7471(76)90879-2.

Polzin, K., N. Oakey, J. Toole, and R. Schmitt, 1996: Fine structure and microstructure characteristics across the northwest Atlantic subtropical front. *J. Geophys. Res.*, **101**, 14 111–14 121, https://doi.org/10.1029/96JC01020.

Rainville, L., and R. Pinkel, 2004: Observations of energetic high-wavenumber internal waves in the Kuroshio. *J. Phys. Oceanogr.*, **34**, 1495–1505, https://doi.org/10.1175/1520-0485(2004)034<1495:OOEHIW>2.0.CO;2.

Scargle, J. D., 1982: Studies in astronomical time series analysis. II—Statistical aspects of spectral analysis of unevenly spaced data. *Astrophys. J.*, **263**, 835–853, https://doi.org/10.1086/160554.

Shakespeare, C. J., and A. M. Hogg, 2017: Spontaneous surface generation and interior amplification of internal waves in a regional-scale ocean model. *J. Phys. Oceanogr.*, **47**, 811–826, https://doi.org/10.1175/JPO-D-16-0188.1.

Shcherbina, A. Y., L. D. Talley, E. Firing, and P. Hacker, 2003: Near-surface frontal zone trapping and deep upward propagation of internal wave energy in the Japan/East Sea.

J. Phys. Oceanogr., **33**, 900–912, https://doi.org/10.1175/1520-0485(2003)33<900:NFZTAD>2.0.CO;2.

Thomas, L. N., 2012: On the effects of frontogenetic strain on symmetric instability and inertia–gravity waves. *J. Fluid Mech.*, **711**, 620–640, https://doi.org/10.1017/jfm.2012.416.

——, C. M. Lee, and Y. Yoshikawa, 2010: The subpolar front of the Japan/East Sea. Part II: Inverse method for determining the frontal vertical circulation. *J. Phys. Oceanogr.*, **40**, 3–25, https://doi.org/10.1175/2009JPO4018.1.

——, J. R. Taylor, E. A. D'Asaro, C. M. Lee, J. M. Klymak, and A. Shcherbina, 2016: Symmetric instability, inertial oscillations, and turbulence at the Gulf Stream Front. *J. Phys. Oceanogr.*, **46**, 197–217, https://doi.org/10.1175/JPO-D-15-0008.1.

van Meurs, P., 1998: Interactions between near-inertial mixed layer currents and the mesoscale: The importance of spatial variabilities in the vorticity field. *J. Phys. Oceanogr.*, **28**, 1363–1388, https://doi.org/10.1175/1520-0485(1998)028<1363:IBNIML>2.0.CO;2.

Weller, R. A., 1982: The relation of near-inertial motions observed in the mixed layer during the JASIN (1978) experiment to the local wind stress and to quasi-geostrophic flow field. *J. Phys. Oceanogr.*, **12**, 1122–1136, https://doi.org/10.1175/1520-0485(1982)012<1122:TRONIM>2.0.CO;2.

Whitt, D. B., 2015: Near-inertial waves in oceanic fronts: From generation to dissipation. Ph.D. thesis, Stanford University, 200 pp.

——, and L. N. Thomas, 2013: Near-inertial waves in strongly baroclinic currents. *J. Phys. Oceanogr.*, **43**, 706–725, https://doi.org/10.1175/JPO-D-12-0132.1.

——, and ——, 2015: Resonant generation and energetics of wind-forced near-inertial motions in a geostrophic flow. *J. Phys. Oceanogr.*, **45**, 181–208, https://doi.org/10.1175/JPO-D-14-0168.1.